Arabian Journal of Chemistry (2022) **15**, 103748

King Saud University

Arabian Journal of Chemistry

www.ksu.edu.sa
www.sciencedirect.com

ORIGINAL ARTICLE

Iron oxide nanoparticles-loaded hyaluronic acid nanogels for MRI-aided Alzheimer's disease theranostics

Xie Chen [a,1], Xiaofeng Guo [a,1], Sha Hao [b,1], Tiejun Yang [c], Junsong Wang [a,*]

[a] *Department of CT/MRI, Wenling First People's Hospital, Wenling 317500, China*
[b] *Department of Oncology, Jingmen Hospital of Traditional Chinese Medicine, Jingmen 448000, China*
[c] *Department of Radiology, Taizhou Municipal Hospital, Taizhou 31800, China*

Received 29 June 2021; accepted 27 January 2022
Available online 1 February 2022

KEYWORDS

Hyaluronic acid nanogels;
Amyloid beta fibrillation;
Alzheimer's disease;
MRI contrast agent;
Theranostic systems

Abstract Despite eye-opening advances in developing novel therapeutics for hard-to-treat diseases, treatment of Alzheimer's disease (AD) is still known as the challenge of generations. By the way, scrutinizing and shedding light on a major cause of AD, i.e., fibrillation of β amyloid (Aβ) peptides, have paved the way to find an effective therapy for this life-threatening disease in the foreseeable future. In this study, we endeavored to push forward with research on AD therapy, even as much as an inch, by fabricating and evaluating a theranostic system based on iron oxide nanoparticles-loaded hyaluronic acid nanogels (Fe_3O_4-HyA NGs). Fe_3O_4 nanoparticles were fabricated via a facile co-precipitation method and were loaded in HyA NGs in situ by formation of NGs using a thiolated HyA (HyA-SH) precursor. Standard structural analysis was performed on Fe_3O_4-HyA NGs, and the results revealed the NGs were negatively charged, which led to relatively poor adsorption of plasma proteins, and sized at the range of 120–150 nm. Also, Fe_3O_4-HyA NGs showed a superparamagnetic property with a magnetic saturation of about 62.8 emu/g indicating the successful loading of Fe_3O_4 nanoparticles. Besides, findings of the cytotoxicity analysis could primarily show the NGs did not pose a noticeable risk to normal astrocyte cells (i.e., 96.7% cell viability at 100 μg/ml after 48 h treatment). Moreover, *in vitro* magnetic resonance imaging (MRI) analysis could reveal the noticeable potential ability of the Fe_3O_4-HyA NGs to generate negative contrast by reducing both T2-weighted and T2*-weighted MR signal intensities with a relaxation

* Corresponding author at: No. 333 Chuan'an South Road, Chengxi Street, Wenling 317599, Zhejiang, China
E-mail address: juns_wang@yahoo.com (J. Wang).
[1] Xie Chen, Xiaofeng Guo, Sha Hao Contributed equally to this study.

Peer review under responsibility of King Saud University.

Production and hosting by Elsevier

https://doi.org/10.1016/j.arabjc.2022.103748

rate (r_2) of about 120.87 (1/mM.sec). Finally, Fe_3O_4-HyA NGs exhibited a potential ability to impede Aβ aggregation by around 44% at 10 μM; also, they could induce disaggregation of Aβ fibrils by about 13% at 10 μM. Hence, Fe_3O_4-HyA NGs could be a promising choice for AD theranostics and could be further scrutinized *in vitro* and *in vivo*.

1. Introduction

"A progressive multifactorial neurodegenerative form of dementia" (Amakiri et al., 2019), this is perhaps the most succinct definition of Alzheimer's disease (AD) which depicts almost all about it: AD is progressive, i.e., the diagnosis should happen as early as possible, and the following treatment should act as fast and efficient as possible. AD is multifactorial, i.e., fighting this disease is not a one battle war, and it requires a comprehensive treatment strategy. AD is neurodegenerative, i.e., it targets the brain tissue which is the hardest to access through systemic administration of therapeutics due to the blood-brain barrier (BBB), so this adds another cumbersome step to the drug development process for AD therapy. Despite tremendous efforts abandoned over the decades by the scientists around the world to heal AD, there is still no definitive cure available for the patients (Tosi et al., 2019). Most recently, the Food and Drug Administration (FDA) of the United States approved the first novel therapeutic, i.e., Aduhelm (aducanumab), for AD treatment since 2003 (Patrizia Cavazzoni, 2021), but there is no guarantee that Aduhelm could be that 100% treatment the world has been expecting for so long.

Nonetheless, there is light at the end of the tunnel, as one of the lead players in initiation and development of AD, fibrillation of β amyloid (Aβ) peptides, has been widely investigated, and there are plenty of data shedding light on different aspects of Aβ aggregation and the consequent effects leading to AD (Amakiri et al., 2019). Not surprisingly, Aduhelm has been actually designed to target Aβ plaques in the brain (Patrizia Cavazzoni, 2021). Aβ comes from amyloid beta precursor protein (APP), and $Aβ_{40}$ and $Aβ_{42}$ are the most abundant species of Aβ (Murphy and LeVine, 2010). Formation of Aβ oligomers from the corresponding monomers poses toxicity to synapses in the brain primarily, and formation Aβ plaques contributes to further development of AD (Mucke and Selkoe, 2012), as a very small plaque formation could give rise to AD pathology (Erten-Lyons et al., 2009). Nanomedicine based therapeutics are among the most promising compounds owing to their unique features, such as ability to bypass the BBB and high selectivity and specificity (Tosi et al., 2019). For instance, Lin et al. designed a nanocarrier based on polyplex nanomicelles for Neprilysin (NEP)-expressing mRNA delivery to brain with the aim of degrading Aβ monomers and oligomers which could lead to a mitigated Aβ aggregation (Lin et al., 2016). Also, the hydrophilicity of their proposed nanocarrier could lead to a prolonged circulation time which could favor bypassing the BBB. In another study by Vilella et al. (Vilella et al., 2018), evaluation of of zinc loaded poly(lactide-co-glycolide) *in vivo* exhibited a noticeable effect on reducing the mean plaque area and inflammation, while the endogenous cheatable zinc was not impacted by the delivered zinc (Vilella et al., 2018). Sun et al. studied a nanomaterial based therapeutic (sulfur; methionine $Na_2S_2O_3$) which could reduce Aβ-Cu^{2+} complex aggregation by 61.6% and enhance cell viability of SH-SY5Y human neuroblastoma by 92.4% *in vitro*; also, their designed nanodrug could effectively cross the BBB *in vivo* (Sun et al., 2018).

Hyaluronic acid (HyA) is a natural polysaccharide with a linear conformation composed of [-4-d-glucuronic acid-β1-3-N-acetylglucosamine-β1-]$_n$. As a non-sulfated glycosaminoglycan, HyA is endogenously synthesized by hyaluronan synthase and is recognized as the main part of the extracellular matrix (Vilella et al., 2018). Also, HyA plays a vital role in preserving the tissue's homeostasis, viscoelasticity, lubrication, and mechanical properties given its high-water absorption capacity and high molecular weight (Sheervalilou et al., 2021). HyA based materials have been widely studied for drug delivery purposes due to their favorable biodegradability, biofunctionality, biocompatibility, and non-immunogenicity (Trombino et al., 2019). It has recently been reported that HyA, as a negatively charged glycosaminoglycan, could impede Aβ fibrillation by targeting the Aβ domain (Jiang et al., 2018).

Iron oxide nanoparticles (Fe_3O_4 NPs) have been extensively investigated and applied for production of drug delivery and theranostic systems owing to several advantages they offer, e.g., favorable biocompatibility, versatility, high magnetic property, size controlled synthesis procedure, ample loading capacity, great function once applied for passive and active targeting, etc. [12]. Also, Fe_3O_4 NPs have been widely used as a negative contrast agent for magnetic resonance imaging (MRI) applications, especially given their unique surface properties which allow a facile surface modification and functionalization using a variety of ligands and coatings leading to their improved performance in creating dark contrast at the site of interest [13]. Hence, Fe_3O_4 NPs are recognized as one the best choices in design on theranostic systems [14].

In this study, Fe_3O_4 NPs-loaded HyA nanogels (Fe_3O_4-HyA NGs) were fabricated and studied for AD theranostics via impeding the aggregation of Aβ, which is recognized as an efficient strategy for AD treatment, and generating a negative contrast once MRI technique is applied for diagnosis purposes. Standard structural analysis of nanomaterials were carried out to evaluate the physicochemical features of the fabricated Fe_3O_4-HyA NGs including chemical structure, size, size distribution, surface charge, and magnetic property. Also, protein corona analysis was done to primarily appraise the interaction of the NGs once exposed to plasma proteins, and cytotoxicity analysis was performed to assess toxicity of the NGs against normal astrocyte cells of the brain tissue. Finally, *in vitro* MRI and Aβ aggregation and disaggregation studies were conducted to primarily investigate the potential ability of the fabricated Fe_3O_4-HyA for AD theranostics. It is worth mentioning that albeit Fe_3O_4 NPs can function against Aβ aggregation (Mahmoudi et al., 2013), their application in this study was only for their capability to

produce negative contrast; furthermore, it was assumed that Fe_3O_4 NPs would mostly remain inside the HyA NGs, so they could not properly interact with Aβ monomers.

2. Materials and methods

2.1. Materials

2.1.1. Chemicals

The majority of the chemicals were procured from Sigma-Aldrich (St. Louis, MO, U.S.A.) and utilized without further purification, except for $FeCl_3{\cdot}6H_2O$, $FeCl_2{\cdot}4H_2O$, sodium hyaluronate 200 kDa, dithiothreitol (DTT), Thiazolyl Blue Tetrazolium Bromide (MTT), and Hexafluoroisopropanol (HFIP), which were purchased from Merck (Darmstadt, Germany) and used without further purification.

2.1.2. Cell culture

Normal astrocyte cells (C8-D1A, ATCC, Rockville, MD, USA) were cultured at a density of 2×10^4 cells/cm^2 RPMI 1640 (Sigma-Aldrich, St. Louis, MO, U.S.A.) media along with 10% heat-inactivated fetal bovine serum (FBS) (Sigma-Aldrich, St. Louis, MO, U.S.A.), streptomycin (Merck, Darmstadt, Germany), and penicillin (Merck, Darmstadt, Germany) under a humid atmosphere (95%) and CO_2 (5%) at 37 °C.

2.2. Methods

2.2.1. Fabrication of Fe_3O_4 NPs

In order to fabricate Fe_3O_4 NPs, a standard chemical co-precipitation method was employed (Zhu et al., 2013). Concisely, $FeCl_3{\cdot}6H_2O$ (4.32 g) and $FeCl_2{\cdot}4H_2O$ (1.6 g) were dissolved in deionized water (10 ml), and the resulting solution was put under vigorous stirring using a mechanical stirrer for 30 min under nitrogen flow. Next, the temperature of the system was set at 70 °C, and an ammonium hydroxide solution (NH_4OH, 25 ml, 28 wt%) was gently added to set the pH at about 11. After a dark precipitate was produced, the stirring was continued at 1800 rpm for 2 h at 70 °C, and to let the remaining ammonia evaporate, the temperature was raised to 85 °C. Finally, fabricated Fe_3O_4 NPs were isolated via a permanent magnet and rinsed with deionized water several times to remove impurities.

2.2.2. Fabrication of Fe_3O_4 NPs-loaded HyA nanogels (Fe_3O_4-HyA NGs)

To fabricate a HyA based NG, HyA was first thiolated according to a previously reported method [17]. Briefly, tetrabutylammonium hydroxide (TBA-OH) was first used to produce HyA-TBA. Next, HyA-TBA was reacted with diethylenetriaminepentaacetic acid (DTPA), di(*tert*-butyl) dicarbonate (Boc2O), and 4-dimethylaminopyridine (DMAP) to form the intermediate DTP-HA. After, 3,3′-dithiopropionic acid (DTDP) along with dithiothreitol (DTT) (as the reducing agent) were applied for esterification of hydroxyl groups of HyA (Fig. 1S, supporting information). The resulting product was collected via a cold ethanol precipitation procedure followed by freeze drying at pH 3.5 [18]. Then, formation of thiolated HyA (HyA-SH) was assessed and confirmed by ^{1}H NMR analysis, as the appearance of the characteristic peak of $-CH_2CH_2SH$ at around $\delta = 2.6$ ppm could indicate the successful thiolation of HyA. Also, based on the Ellman's method [19], the thiolation degree (i.e., molar ratio (%) of attached thiol molecules to the number of repeating units of HyA) was determined about 11.5%. Next, Fe_3O_4 NPs-loaded HyA nanogels (Fe_3O_4-HyA NGs) were fabricated as follows [20]: aqueous solutions of HyA-SH and Fe_3O_4 NPs were prepared by dissolving 100 mg of each in 50 ml of deionized water. After, the obtained solutions were mixed and stirred at 100 rpm for around 2.5 h to allow the fabrication of Fe_3O_4-HyA NGs with a narrow size distribution as much as possible. Finally, the obtained suspension was rinsed with ethanol and deionized water for several times using centrifugation at 8000 rpm for 15 min, and the resulting Fe_3O_4-HyA NGs were redispersed in deionized water and kept at 4 °C.

2.2.3. Characterization analysis

Fourier transform infrared (FT-IR) spectrum of Fe_3O_4 NPs was obtained via a Magna 550, Nicolet spectrometer at 500–4000 cm^{-1}. The X-ray diffraction (XRD) pattern of Fe_3O_4 NPs was determined by a Shimadzu XRD 6000 diffractometer. Surface charge and hydrodynamic size distribution of the samples were investigated through dynamic light scattering (DLS) and Zeta potential analysis in deionized water at room temperature via Zetasizer (ZEN3600, Malvern). Size and morphology of the Fe_3O_4 NPs and Fe_3O_4-HyA NGs were evaluated by a scanning electron microscope (SEM) (Tescan Mira LMU) and transmission electron microscope (TEM) (CM30, Philips), respectively. Magnetic properties of the fabricated samples were assessed by a vibrating sample magnetometer (VSM) method using an MPMS3 Quantum Design SQUID magnetometer at 25 °C. ^{1}H NMR analysis was performed to ensure the successful thiolation of HyA by Ascend 400TM, Bruker. Inductively coupled plasma mass spectrometry (ICP-MS) analysis was conducted to determine Fe concentration of the samples by a 7900, Agilent instrument for *in vitro* MRI analysis. Synergy™ LX Multi-Mode Microplate Reader (BioTek) was used to obtain fluorescence spectra.

2.2.4. Protein corona analysis

Sodium Dodecyl Sulfate Polyacrylamide Gel Electrophoresis (SDS-PAGE) method was applied to assess the formation protein corona on the surface of the fabricated Fe_3O_4-HyA NGs (Sakulkhu et al., 2014). Briefly, 0.9 ml of human plasma solutions at concentrations of 10% and 100% were prepared in four 1.5 ml vials. Plasma dilution was done via a phosphate-buffered saline (PBS) solution at pH 7.4. Next, Fe_3O_4 NPs and Fe_3O_4-HyA NGs colloidal solutions (0.1 ml, 1 mg/ml) were added to the prepared human plasma solutions, and the final solutions were incubated at 37 °C for 1 h to allow maximum plasma proteins adsorption on the surface of samples. Then, the solutions were centrifuged at 11,000 rpm for 30 min, and the supernatants were replaced with PBS (0.5 ml, pH 7.4) to remove unbound plasma proteins from the medium. Protein corona determination by SDS-PAGE was performed as follows: the extracted corona proteins from the Fe_3O_4 NPs and Fe_3O_4-HyA NGs samples were first mixed with the sample buffer of [Tris HCl (125 mM); pH 6.8; SDS (4% w/v); glycerol (20% w/v); 2-mercaptoethanol (5% w/v) and bromophenol blue (0.06% w/v)]. Next, the obtained

a)

	Diam. (nm)	% Intensity	Width (nm)
Z-Average (d. nm): 154.1	Peak 1: 162.3	100.0	7.854
PdI: 0.241	Peak 2: 0.00	0.0	0.00
Intercept: 0.832	Peak 3: 0.00	0.0	0.00

c)

	Mean (mV)	Area (%)	Width (mV)
Zeta Potential (mV): -27.8	Peak 1: -27.8	100.0	4.95
Zeta Deviation (mV): 4.04	Peak 2: 0.00	0.0	0.00
Conductivity (mS/cm): 0.153	Peak 3: 0.00	0.0	0.00

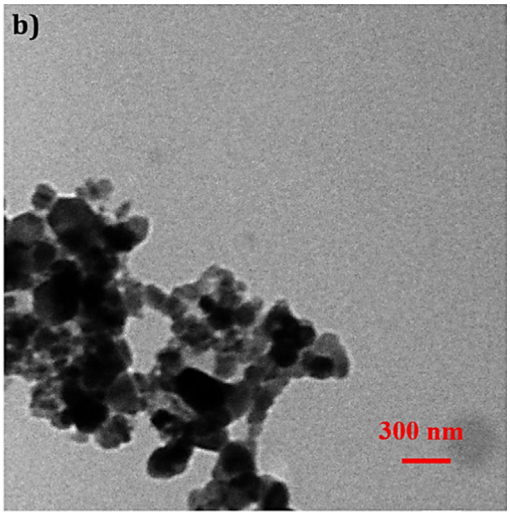

Fig. 1 a) DLS data showing the average size and size distribution of Fe_3O_4-HyA NGs. b) TEM image of spherical Fe_3O_4-HyA NGs. c) Zeta potential data of negatively charged Fe_3O_4-HyA NGs.

mixtures were boiled at 100 °C for 10 min. The separation process was then conducted by placing equal volumes of the samples on 12% acrylamide SDS-PAGE for ~90 min run at 120 V. Eventually, acidic silver nitrate staining protocol was employed to detect the separated proteins, and GelAnalyzer 19.1 software was applied to analyze gel densitometry.

2.2.5. MTT analysis

To study safety of Fe_3O_4-HyA NGs for normal cells, their cytotoxicity against normal astrocyte cells (C8-D1A) was studied via a standard MTT (3-(4, 5-dimethyl thiazol-2-yl)-2, 5-diphenyl tetrazolium bromide) analysis (Bigdeli et al., 2016). In summary, C8-D1A cells were seeded in 96-well plates at the density of 7×10^3 cells/well using 200 µl of RPMI medium followed by incubation for 24 h to allow them attach perfectly. Next, the media were replaced with fresh media including Fe_3O_4-HyA NGs dispersed in deionized water at concentrations of 10, 50, and 100 µg/ml, where the total volume of each medium was 200 µl. Afterwards, the plates were incubated at 37 °C for 24 and 48 h. Then, 100 µl of a PBS solution including MTT (0.5 mg/ml) was added to each well. A Bio Tek microplate reader (USA) was employed to determine the absorbance of each well at the test wavelength of 570 nm and the reference wavelength of 630 nm. Cell viability was calculated based on the following equation (Eq. (1)):

$$Number\ of\ viable\ cell = \frac{Absorbance\ of\ sample}{Absorbance\ of\ control} \times 100 \qquad (1)$$

The results were reported as the mean value ± SD of three independent assays.

2.2.6. In vitro MRI analysis

A phantom imaging method was applied to evaluate the diagnostic capability of the fabricated Fe_3O_4-HyA NGs as compared to Fe_3O_4 NPs as MRI contrast agents (Zhang et al., 2012). In this regard, phantom agar gel samples of Fe_3O_4 NPs and Fe_3O_4-HyA NGs at Fe concentrations of 0–1.28 mM were prepared using agar solution (2.5% w/v) in PBS (0.1 M, pH 7.4). Next, a Bruker Biospec 3T MRI scanner was utilized to achieve T2 and T2* weighted images of the above samples given the below MRI parameters:

For T2-weighted images: TR = 2000 ms, TE = 22, 44, 66, 88, 110, 132, 154, 176, 198, 220, 242, 264, 286, 308, 330, and 352 ms, FOV = 200 mm × 200 mm, slice thickness = 5 mm, and matrix = 192 × 256.

For T2*-weighted images: TR = 391 ms, TE = 2.6, 4.6, 6.6, 10.6, 12.6, 14.6, and 16.6 ms, FOV = 200 mm × 200 mm, slice thickness = 5 mm, and matrix = 192 × 192.

T2 values were determined via a T2 mapping sequence using the above-mentioned parameters. Also, the slope of a linear fit of Fe concentration (mM (versus 1/T2 (s^{-1}) was reported as the T2 relaxation rate (r2).

2.2.7. Aβ aggregation and disaggregation analysis

To evaluate the impact of the fabricated Fe_3O_4-HyA NGs on Aβ aggregation and disaggregation, an $A\beta_{42}$ sample was prepared at first as follows (Zagorski et al., 1999): a 1 mg/ml solution of the peptide in trifluoroacetic acid (TFA) was prepared via sonication for 10 min; then, the solution was put under nitrogen flow to let the TFA evaporate. Next, HFIP (1 ml) was added, and the resulting solution was incubated for 1 h at 37 °C and then dried under nitrogen flow. The above protocol was done two more times. After, HFIP (1 ml) was applied to dissolve the dried peptide followed by fast-freezing at −80 °C. Then, the sample was freeze-dried for about 10 h, and the resulting material was added to a 5 mM NaOH solution in deionized water (1.5 mM) and kept at −80 °C.

Aβ aggregation in the presence of Fe_3O_4-HyA NGs was studied as follows (Oliveri et al., 2015): Fe_3O_4-HyA NGs (at concentrations of 0.5, 1, 5, and 10 µM), thioflavin T (ThT, 45 µM), and $A\beta_{42}$ (15 µM) were placed under incubation in a 50 mM MOPS ((3-(N-morpholino)propanesulfonic acid)) buffer solution (pH 7.4) in a multiplate reader at 37 °C. Next, excitation and emission wavelengths at 450 nm and 480 nm, respectively, were recorded in triplicate. The obtained results were reported as mean ± SD. In addition, to do a brief kinetic evaluation on the inhibitory effect of Fe_3O_4-HyA NGs against Aβ aggregation at the concentration of 10 µM, the obtained

excitation and emission values were fitted to (Eq. (2)), so that F_{max} - F_0 was the maximum fluorescence outcome resulted from Aβ aggregation, and the lag time ($t_{lag} = t_{1/2}–2\,k$) was the delay time prior to creation of ThT-sensitive amyloid species. For more information please see (Oliveri et al., 2015; Greco et al., 2020).

$$F(t) = F0 + \frac{Fmax - F0}{1 + e^{-\frac{t - t1/2}{k}}} \quad (2)$$

Aβ disaggregation induced by Fe_3O_4-HyA NGs was assessed as follows (Greco et al., 2020): to allow proper aggregation of $Aβ_{42}$ prior to introduction of Fe_3O_4-HyA NGs, two $Aβ_{42}$ (15 μM) and ThT (45 μM) containing solutions were incubated in 50 mM MOPS buffer solution (pH 7.4) for 40 h at 37 °C using a black 96-well plate. Then, two solutions of Fe_3O_4-HyA NGs (5 and 10 μM) were introduced to the above solutions and kept in a multiplate plate for 24 h at 37 °C to allow proper interaction of Fe_3O_4-HyA NGs with the previously formed Aβ fibrils. ThT fluorescence emission at 480 nm upon excitation at 450 nm was recorded to determine Aβ disaggregation by calculating the percentage of drop in ThT upon introduction of Fe_3O_4-HyA NGs.

3. Results and discussion

Fe_3O_4-HyA NGs were fabricated for AD theranostics. The NGs were first studied structurally through some standard analysis of nanomaterials to ensure their physicochemical properties are in line with the biomedical applications proposed for them; then, their capabilities were assessed to function as negative MRI contrast agents and to impede Aβ aggregation simultaneously.

3.1. Structural characterization of Fe_3O_4 NPs

The successful fabrication of Fe_3O_4 NPs was first investigated via FT-IR analysis. The obtained FT-IR spectrum of Fe_3O_4 NPs showed three characteristic peaks of stretching Fe - O bond at 610 cm^{-1}, –OH deformed vibration at 1668 cm^{-1}, and stretching –OH at 321 cm^{-1}, which could primarily confirm the successful fabrication of Fe_3O_4 NPs (Bordbar et al., 2014, 2014). Next, XRD analysis was performed to study the crystalline structure of Fe_3O_4 NPs. As depicted in the XRD pattern acquired for Fe_3O_4 NPs (Fig. 2S), six characteristic peaks attributed to Fe_3O_4 NPs appeared at 2θ of 31°, 36. °, 44°, 53°, 57°, and 62° which could be ascribed to planes of (220), (311), (400), (422), (511), and (440), respectively; hence, given the reference standard peaks of Fe_3O_4 NPs (JCPDS card 72-2303) (Schweiger et al., 2011), it could be concluded that Fe_3O_4 NPs were successfully fabricated.

In addition, to evaluate the size, size distribution, morphology, and surface charge of the fabricated Fe_3O_4 NPs, standard DLS, SEM, and Zeta potential analysis were conducted. Fig. 3Sa and 4Sb exhibit the SEM image and DLS data of Fe_3O_4 NPs, so that the mean diameter of the NPs was determined 28 nm with a relatively narrow size distribution and polydispersity index (PDI) of 0.253. Also, as seen in the SEM image, the size of the fabricated Fe_3O_4 NPs was about 22 nm, and they were spherical with an even size distribution. The difference between the size of the NPs obtained from DLS and SEM analysis could be due to the fact the DLS was performed in an aqueous medium, while SEM was done on the dried sample of Fe_3O_4 NPs. Moreover, as depicted in Fig. 3Sc, the Zeta potential of Fe_3O_4 NPs was determined about – 5.3 (mv) which could be ascribed to the negative charge of hydroxyl groups covering the surface of the NPs.

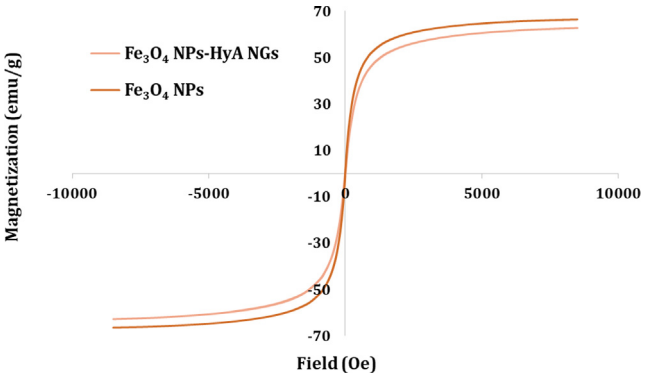

Fig. 2 Superparamagnetic property of Fe_3O_4 NPs and Fe_3O_4-HyA NGs examined by VSM analysis.

3.2. Structural characterization of Fe_3O_4-HyA NGs

To confirm the successful fabrication of Fe_3O_4-HyA NGs, we needed to check their size, morphology, surface charge, and superparamagnetic magnetic property. Hence, the DLS analysis was initially performed to evaluate the NGs' size and size distribution. As seen in Fe_3O_4-HyA NGs' DLS data (Fig. 1a), their mean diameter was determined around 154 nm with a PdI of 0.241. Next, the TEM analysis was done to further scrutinize the morphology of the NGs, so as shown in Fig. 1b, the fabricated Fe_3O_4-HyA NGs appeared spherical with the mean diameter of 125 nm. Since the TEM analysis was also performed on the dried samples of NGs, the difference in the results of DLS and TEM analysis was no surprise (please see the section 3.1.). It has been previously reported that particle size < 250 nm favors targeted drug delivery in case of intravenous administration [29], so it could be concluded that the size of fabricated Fe_3O_4-HyA NGs was in favor of their proposed application for AD theranostics. Besides, the size stability of Fe_3O_4-HyA NGs in PBS (pH 7.4) was examined, and as shown in Fig. 4S, the particle size of the NGs gradually decreased by about 14% over 7 days in fridge, which almost did not result in release of Fe_3O_4 NPs. Also, no considerable change was observed in the size of Fe_3O_4-HyA NGs after 14 days in the same condition (data not shown). It has been previously reported that HyA based hydrogels with a molecular weight at the range of 200–300 kDa show a noticeable resistance against long-term degradation [30].

Furthermore, the Zeta potential analysis revealed that the Fe_3O_4-HyA NGs had a negative surface charge of about – 27.8 (mv) (Fig. 1c) which could be ascribed to the negative charge of HyA-SH as the building block of the NGs (Tian et al., 2018). It has been shown in previous studies that negatively charged nanobiomaterials, as compared to positively charged ones, introduce the advantage of longer blood circulation, as the absorbance of plasma proteins onto their surface is relatively insignificant which leads to a less clearance rate from blood circulation (Honary and Zahir, 2013).

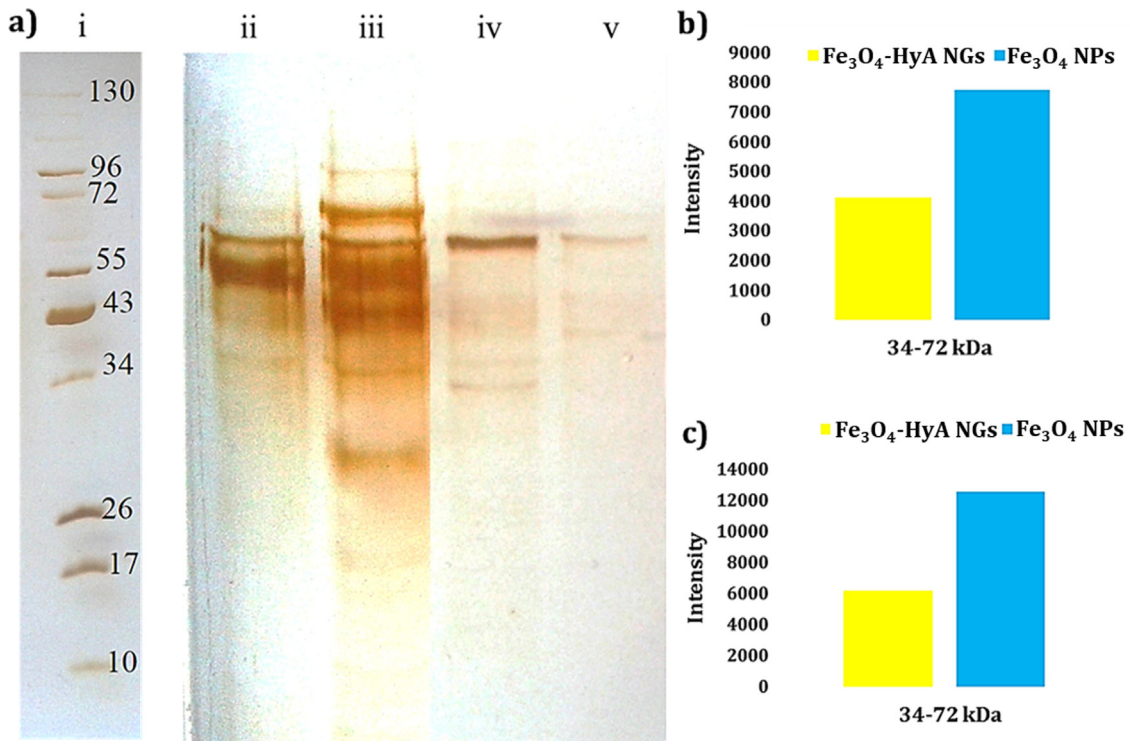

Fig. 3 a) Photo of the SDS-PAGE gel of plasma proteins interacted with (ii) Fe_3O_4 NPs and (v) Fe_3O_4-HyA NGs at 10% concentration of plasma; and (iii) Fe_3O_4 NPs and (iv) Fe_3O_4-HyA NGs at 100% concentration of plasma representing *in vitro* and *in vivo* media, respectively. Also, the reference ladder showing the molecular weights of the proteins is marked by (i). The contrast of this photo was enhanced to achieve a better visualization of the protein bands. b) and c) Histograms illustrating the corresponding intensity of the adsorbed plasma proteins (at a molecular weight range of 34–72 kDa) at 10% and 100% plasma concentrations, respectively.

So far so good. Yet we needed to ensure the successful loading of Fe_3O_4 NPs in the HyA NGs which was supposed to render a superparamagnetic magnetic property to the Fe_3O_4-HyA NGs. Therefore, a VSM analysis was carried out to assess the magnetic property of Fe_3O_4-HyA NGs in comparison with Fe_3O_4 NPs. As shown in Fig. 2, both Fe_3O_4 NPs and Fe_3O_4-HyA NGs demonstrated a superparamagnetic magnetic property, as neither coercivity nor remanence of the hysteresis loops was detected in the obtained graphs. Besides, magnetic saturation values of Fe_3O_4 NPs and Fe_3O_4-HyA NGs were respectively determined about 66.4 and 62.8 emu/g, which not only could indicate the successful loading of a considerable amount of Fe_3O_4 NPs in the HyA NGs, but it also could reveal that Fe_3O_4 NPs encapsulation did not noticeably affect the resulting magnetic property for Fe_3O_4-HyA NGs (Su et al., 2019), so they could be studied as a potential MRI contrast agent.

3.3. Protein corona analysis

To find out what happens at the nano-bio interface has significantly drawn the attention of scientists recently, as it noticeably impacts the function of nanobiomaterials via several ways once introduced to the human body (Mahmoudi, 2018). Hence, as a primary test, the formation of protein corona on the surface of the Fe_3O_4-HyA NGs was studied through a standard protein corona analysis in which 10% and 100% concentrations of human plasma were applied to represent *in vitro* and *in vivo* media, respectively (Fig. 3a) (Sakulkhu et al., 2014). Also, the obtained results were compared with those of Fe_3O_4 NPs. As it could be expected given the noticeably negative surface charge of Fe_3O_4-HyA NGs relative to Fe_3O_4 NPs, the adsorption of plasma proteins on the surface of the NGs was much less, as it could be observed by the poorly intensive protein bands appeared on the gel. By the way, it should be mentioned that plasma proteins with molecular weights of 34–72 kDa were more adsorbed (Fig. 3b and 3c). In line with the results of Zeta potential analysis, protein corona results could provide further evidence that the fabri-

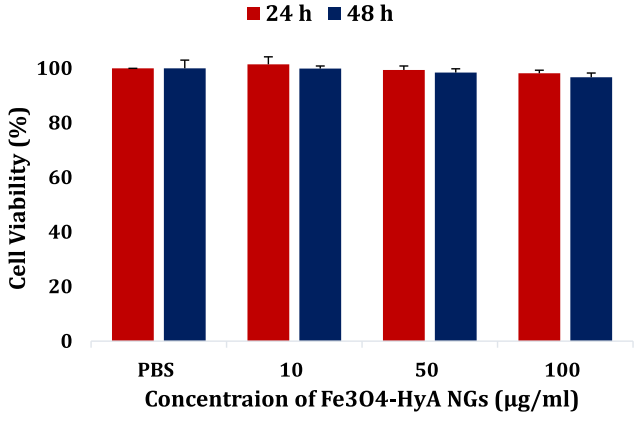

Fig. 4 Cell viability of a normal astrocyte cell line (C8-D1A) treated with Fe_3O_4-HyA NGs for 24 h and 48 h. The data were reported as the mean value ± SD of three independent assays.

cated Fe_3O_4-HyA NGs might possibly show a prolonged blood circulation time which could favor their biomedical function. However, more *in vitro* and *in vivo* analysis are to be performed to support this idea.

3.4. MTT analysis

The potential target tissue of the fabricated Fe_3O_4-HyA NGs would be the brain tissue; hence, to primarily investigate the cytotoxicity of the NGs against normal cells, a normal astrocyte cell line (C8-D1A) was incubated with Fe_3O_4-HyA NGs, and the cell viability study was done through a standard MTT analysis. As illustrated in Fig. 4, Fe_3O_4-HyA NGs showed almost no cytotoxicity against C8-D1A, as at the top concentration of the NGs (i.e., 100 μg/ml) the determined cell viability values were 98.2% and 96.7% for 24 and 48 h of treatment, respectively. These results were not unexpected because HyA has been known as a safe, biocompatible natural compound favorable for biomedical applications (Trombino et al., 2019; Seliktar, 2012; Li and Mooney, 2016; Snetkov et al., 2020). Also, if Fe_3O_4 NPs get released from the NGs' structure in any case, they could not pose a significant risk to normal cells, as it has been widely recognized that Fe_3O_4 NPs are among the safest nanomaterials for nanomedicine applications (Arias et al., 2018; Dulińska-Litewka et al., 2019).

3.5. In vitro MRI analysis

As revealed by the VSM analysis results, Fe_3O_4-HyA NGs showed a noticeable magnetic property which could favor their application as an MRI contrast agent. Along with the developments on design and production of novel therapeutics for hard-to-treat diseases, such as AD, cancer, etc., developing effective, accurate diagnostic methods have become a matter of crucial importance since a meticulous diagnosis paves the way for a high throughput treatment. Thus, we performed an *in vitro* MRI analysis on Fe_3O_4-HyA NGs and compared the obtained qualitative (i.e., the MRI images of the samples in PBS at pH 7.4) and quantitative (i.e., T2 values of protons in aqueous solutions of the samples in PBS at pH 7.4) results with those of Fe_3O_4 NPs as a renowned negative contrast agent for MRI applications (Wang, 2011).

Based on the obtained T2-weighted MRI images (Fig. 5a), application of both samples led to a dark negative contrast in comparison with the control sample. More importantly, Fe_3O_4-HyA NGs could noticeably reduce T2-weighted magnetic resonance (MR) signal intensity as compared to Fe_3O_4 NPs at all examined concentrations of Fe. These MRI images could primarily confirm the potential ability of Fe_3O_4-HyA NGs to create negative contrast, yet further quantitative data were needed to provide more evidence in this regard. Hence, r_2 relaxation rate (1/mM.sec) values were calculated to further scrutinize the ability of Fe_3O_4-HyA NGs to reduce signal intensity and generate negative contrast (Fig. 5b and 5c). As seen, for Fe_3O_4 NPs and Fe_3O_4-HyA NGs, the r_2 were respectively calculated 69.56 and 120.87 (1/mM.sec), which could reveal that loading of Fe_3O_4 NPs in HyA NGs could give rise to a considerable rise in the obtained r_2 value and thus a noticeable enhancement in negative contrast generation.

Furthermore, studying the alterations of signal intensity versus TE values for the applied samples could lend further support to the above-mentioned data. Thus, as depicted in Fig. 6a and 6b, signal intensity reduction curves versus increasing TE values could demonstrate the considerable potential capability of Fe_3O_4-HyA NGs to reduce signal intensity, especially at 0.64 and 1.28 mM concentration of Fe, relative to Fe_3O_4 NPs. It was also concluded that there was a nonlinear relationship between signal intensity alterations and the resulted r_2 values.

Based on the obtained results, Fe_3O_4-HyA NGs not only could generate negative contrast with a relatively high r_2 value and a noticeable reduction in signal intensity versus TE, but they exhibited a much better potential ability to be applied as an MRI contrast agent as compared to Fe_3O_4 NPs. As previously discussed in a study by Su et al. (Su et al., 2019), the probable reason behind these results could be a smaller water diffusion coefficient and a rise in the transverse relaxation rated stemmed from encapsulation of Fe_3O_4 NPs in HyA NGs. Nevertheless, meticulous *in vivo* MRI analysis are required to further assess these results and shed light on the fundamental reasons leading to such an interesting effect.

The potential ability of Fe_3O_4-HyA NGs to reduce T2*-weighted MR signal intensity was also investigated and compared with that of Fe_3O_4 NPs. Heterogeneity in the main magnetic field results in T2*-weighted MRI images which is applied diagnosis of disease in heterogeneous tissues. In case of T2*-weighted MRI, signal intensity reduction happens faster than T2, so the T2* relaxation time is known as effective T2 (Shevtsov et al., 2014; Chavhan et al., 2009). As depicted in Fig. 7 and in line with the T2-weighted MRI images, both Fe_3O_4 NPs and Fe_3O_4-HyA NGs could cause negative contrast, as the contrast generated by Fe_3O_4-HyA NGs was more intense at all concentrations of Fe except for 0.04 and 0.08 mM at which the generated contrast by both samples was not that conceivable.

3.6. Aβ aggregation and disaggregation analysis

Aggregation of Aβ, which is initiated with the formation of toxic oligomers, plays an important role in the onset of AD, so it is a momentous matter to curb or impede Aβ aggregation timely and effectively (Murphy and LeVine, 2010). As reported in a recent study by Greco et al. (Greco et al., 2020), HyA with a molecular weight of 200 kDa could prevent Aβ aggregation; thus, in the current study, HyA (200 kDa) was selected to fabricate HyA NGs, so we could compare the obtained results with those of a prominent study. To detect the anti-aggregation function of Fe_3O_4-HyA NGs, ThT was applied as a fibril-sensitive dye.

As illustrated in Fig. 8a, application of Fe_3O_4-HyA NGs could lead to abatement of the fluorescence value by about 44% at the concentration of 10 μM as compared to the control ($A\beta_{42}$, 15 μM). Also, it could be noticed that the anti-aggregation impact of Fe_3O_4-HyA NGs was dose-dependent, as the fluorescence value gradually dropped by an increase in the concentration of Fe_3O_4-HyA NGs from 0.5 μM to 10 μM. The obtained results were satisfactorily in line with the results reported by Greco et al. (Greco et al., 2020). In spite of the studies reporting Aβ fibril formation induced by negatively charged glycosaminoglycans (Valle-Delgado et al., 2010), such as HyA, there is a research which has reported prevention of fibril formation upon introduction of HyA to the

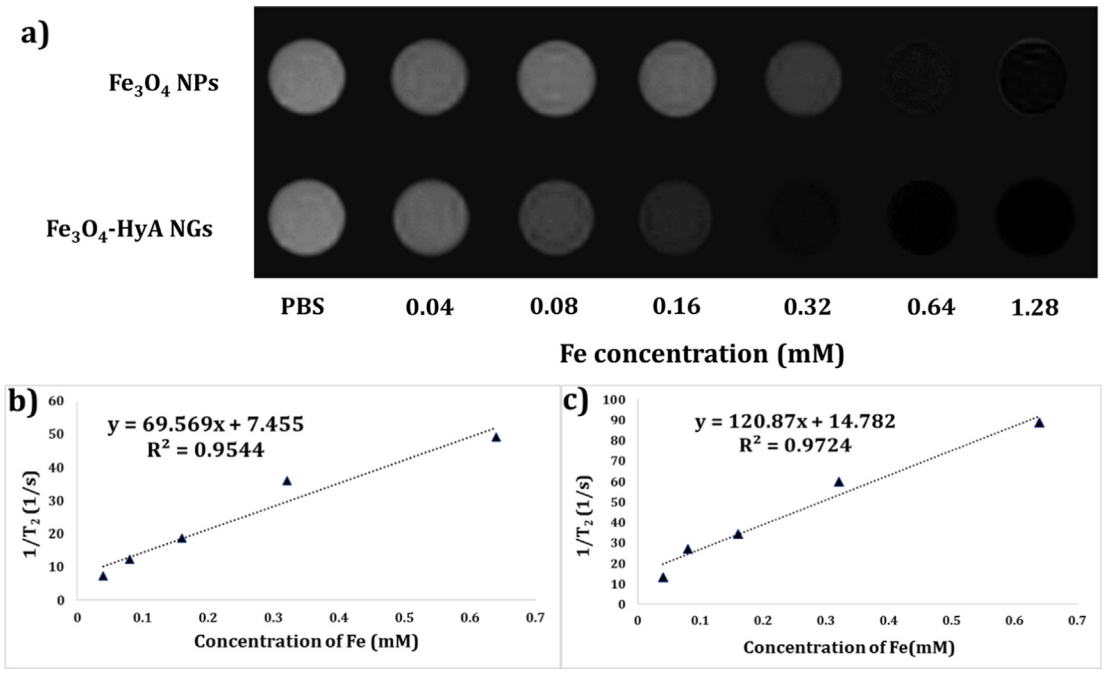

Fig. 5 a) T2-weighted MRI images of colloidal dispersions of Fe_3O_4 NPs and Fe_3O_4-HyA NGs at diverse Fe concentrations showing a dose-dependent dark contrast generation *in vitro*. b) and c) Relaxation (r_2) values reported as the slop of the linear fitting for Fe_3O_4 NPs and Fe_3O_4-HyA NGs, respectively, by plotting (1/T2) values against Fe concentrations.

test medium (Ariga et al., 2010). It has been shown that negative glycosaminoglycans target the Aβ domain encompassing a contiguous tyrosine and a basic residue cluster (HHQK) (Valle-Delgado et al., 2010). Moreover, in a study by Jiang et al. (Jiang et al., 2018), application of HyA was found to noticeably improve the anti-aggregation function of polyphenols to inhibit Aβ fibril formation, as they concluded that formation of HyA conjugate nanogels could impede the interactions between Aβ molecules via causing an isolation effect. Furthermore, Fig. 8b depicts the kinetic trend of Aβ aggregation with and without applying Fe_3O_4-HyA NGs (10 μM). Based on the results, the F_{max} - F_0 value for Fe_3O_4-HyA NGs was determined 18.11 ± 0.60 with a t_{lag} of 5.59 ± 0.70, while for the control sample F_{max} - F_0 value was 50.42 ± 0.70, and t_{lag} was 5.88 ± 0.50. As the Fe_3O_4-HyA

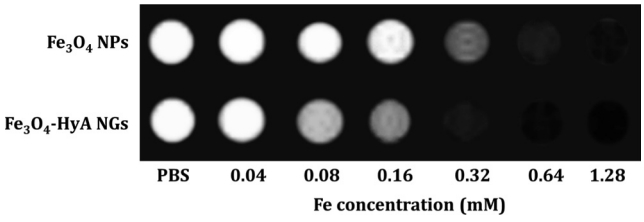

Fig. 7 T2*-weighted MRI images of colloidal dispersions of Fe_3O_4 NPs and Fe_3O_4-HyA NGs at various concentrations of Fe illustrating the potential ability of the fabricated NGs to generate negative contrast *in vitro* at smaller TE values relative to T2-weighted MRI.

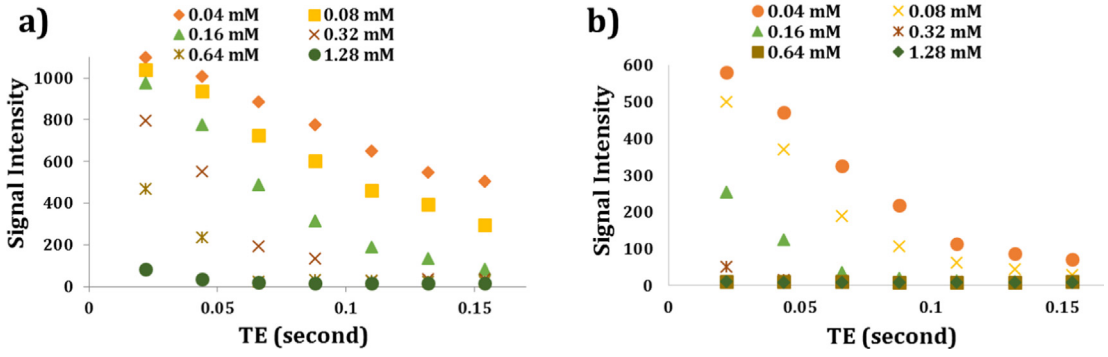

Fig. 6 Graphs showing the potential ability of Fe_3O_4 NPs (a) and Fe_3O_4-HyA NGs (b) to reduce MR signal intensity at different Fe concentrations as the TE values increased *in vitro*.

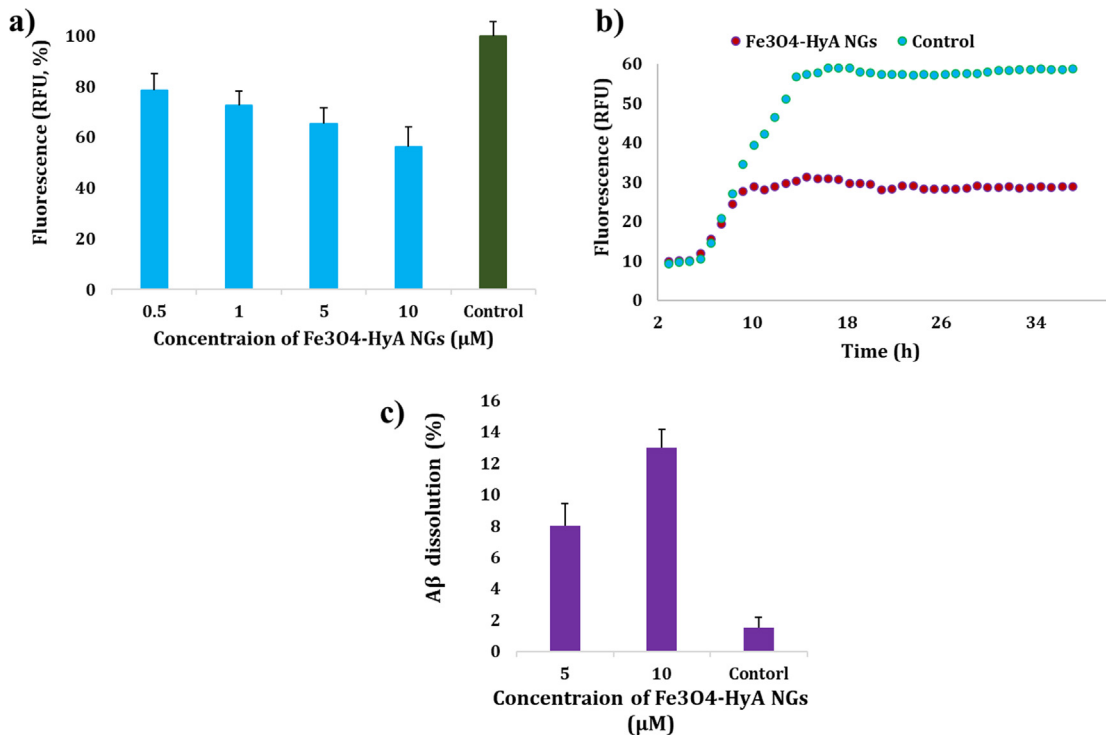

Fig. 8 a) Potential ability of the fabricated Fe_3O_4-HyA NGs to prevent Aβ aggregation as compared to the control ($A\beta_{42}$, 15 μM) *in vitro* indicated by a drop in relative fluorescence values in a dose-dependent manner. b) Kinetic trend of Aβ aggregation with and without using Fe_3O_4-HyA NGs (10 μM) relative to the control ($A\beta_{42}$, 15 μM). c) Fe_3O_4-HyA NGs could relatively induce disaggregation of $A\beta_{42}$ aggregates at two concentrations of 5 and 10 μM *in vitro*. The data (a, b) were reported as the mean value ± SD of three independent assays.

NGs showed a lower F_{max} - F_0 value, it could be further concluded that the fabricated NGs were able to inhibit Aβ aggregation (Oliveri et al., 2015).

In addition, the effect of Fe_3O_4-HyA NGs on disaggregation of Aβ fibrils was investigated in this study by recording the drop in ThT, and it was found that Fe_3O_4-HyA NGs could disaggregate Aβ fibrils by about 8% and 13% at the concentrations of 5 and 10 μM, respectively (Fig. 8c).

As a result, the findings of this study may further encourage researchers to further dig into the potential ability of HyA based nano/hydrogels for AD treatment by using HyA at different molecular weights and confirmations.

4. Conclusion

It literally goes without saying that how much the AD has affected human beings' life worldwide and how much efforts have been made over the decades to prevent and/or treat this life-threatening disease. However, there is still no a 100% treatment for AD, so researchers are working tirelessly to find novel therapeutics which could effectively target the formation of Aβ fibrils as the major cause of AD. Also, as simultaneous therapy and diagnosis has been found to offers several advantages leading to design and develop a more effective treatment strategy, development of a theranostic system for AD treatment could be an improvement. Therefore, in this study, we fabricated and studied Fe_3O_4 NPs loaded HyA NGs (Fe_3O_4-HyA NGs) for AD theranostics. Based on the obtained results from the structural characterization analysis, Fe_3O_4 NPs with the mean diameter of about 22 nm were successfully fabricated and loaded in HyA NGs in situ. The fabricated Fe_3O_4-HyA NGs had a mean diameter of about 125 nm with a Zeta potential value of about –27.8 (mv). Furthermore, Fe_3O_4-HyA NGs showed a noticeable superparamagnetic property with a magnetic saturation value of about 62.8 emu/g favorable for MRI applications, which could also indicate the successful loading of Fe_3O_4 NPs in HyA NGs. Protein corona analysis could reveal that Fe_3O_4-HyA NGs slightly adsorbed plasma proteins which might stem from their negative surface charge and could result in a prolonged blood circulation time. Also, it was found from the MTT analysis that Fe_3O_4-HyA NGs could pose almost no risk (i.e., 96.7% cell viability after 48 h treatment at the NGs' concentration of 100 μg/ml) to normal astrocyte cells (C8-D1A) which could primarily indicate the safety of Fe_3O_4-HyA NGs to be administered to the brain tissue. This result was no surprise, as safety of HyA as a natural, biocompatible material has been widely recognized. Furthermore, *in vitro* MRI results demonstrated that Fe_3O_4-HyA NGs could generate a negative contrast by reducing T2-weighted MR signal intensity (and also T2*-weighted MR signal intensity) with an r_2 value of about 120.87 (1/mM.sec) which was 1.73-fold greater than that of Fe_3O_4 NPs. So, it was concluded that Fe_3O_4-HyA NGs could be further scrutinized as a promising MRI contrast agent. Finally, the potential ability of Fe_3O_4-HyA NGs to impede the aggregation of Aβ and induce disaggregation of Aβ fibrils

was assessed, and it was realized that Fe_3O_4-HyA NGs could prevent Aβ aggregation by about 44% at the concentration of 10 μM relative to the control ($A\beta_{42}$, 15 μM) and also could bring about a relative Aβ fibril disaggregation equal to about 8% and 13% at the concentrations of 5 and 10 μM, respectively. As a result, our findings could provide further evidence on the potential ability of HyA based materials, especially nanomaterials, to inhibit Aβ aggregation which could be effective for AD treatment. Moreover, these results may encourage researchers to further study the design and development of theranostic systems based on HyA NGs, especially for AD theranostics. Nevertheless, a broad *in vivo* analysis is to be carried out meticulously to appraise the validity of the above-mentioned results.

5. Ethics approval and consent to participate

All procedures were carried out in accordance with the Regulations of Experimental Administration issued by the State Committee of Science and Technology of the People's Republic of China, with the approval of the Ethics Committee in our university.

6. Consent for publication

The authors declare consent for application.

Declaration of Competing Interest

The authors declare that they have no known competing financial interests or personal relationships that could have appeared to influence the work reported in this paper.

Appendix A. Supplementary data

Synthesis procedure of HyA-SH, 1H NMR spectrum of HyA-SH, size stability graph of Fe3O4-HyA NGs, and characterization data of Fe3O4 NPs have been provided in the supporting information file. Supplementary data to this article can be found online at https://doi.org/10.1016/j.arabjc.2022.103748.

References

Amakiri, N., Kubosumi, A., Tran, J., Reddy, P.H., 2019. Amyloid Beta and MicroRNAs in Alzheimer's Disease. Front. Neurosci. 13, 430.

Arias, L.S., Pessan, J.P., Vieira, A.P.M., de Lima, T.M.T., Delbem, A. C.B., Monteiro, D.R., 018. Iron Oxide Nanoparticles for Biomedical Applications: A Perspective on Synthesis, Drugs, Antimicrobial Activity, and Toxicity, Antibiot. (Basel, Switzerland). 7, 46.

Ariga, T., Miyatake, T., Yu, R.K., 2010. Role of proteoglycans and glycosaminoglycans in the pathogenesis of Alzheimer's disease and related disorders: Amyloidogenesis and therapeutic strategies—A review. J. Neurosci. Res. 88, 2303–2315.

Bigdeli, B., Goliaei, B., Masoudi-khoram, N., Jooyan, N., Nikoofar, A., 2016. Enterolactone : A novel radiosensitizer for human breast cancer cell lines through impaired DNA repair and increased apoptosis. Toxicol. Appl. Pharmacol. 313, 180–194.

Bordbar, A.K., Rastegari, A.A., Amiri, R., Ranjbakhsh, E., Abbasi, M., Khosropour, A.R., 2014,. Characterization of modified magnetite nanoparticles for albumin immobilization. Biotechnol. Res. Int., 705068

Chavhan, G.B., Babyn, P.S., Thomas, B., Shroff, M.M., Haacke, E. M., 2009. Principles, techniques, and applications of T2*-based MR imaging and its special applications. Radiographics 29, 1433–1449.

Dadfar, S.M., Roemhild, K., Drude, N.I., von Stillfried, S., Knüchel, R., Kiessling, F., Lammers, T., 2019. Iron oxide nanoparticles: Diagnostic, therapeutic and theranostic applications. Adv. Drug Deliv. Rev. 138, 302–325.

Dulińska-Litewka, J., Łazarczyk, A., Hałubiec, P., Szafrański, O., Karnas, K., Karewicz, A., 2019. Superparamagnetic Iron Oxide Nanoparticles-Current and Prospective Medical Applications, Mater. (Basel, Switzerland). 12, 617.

Erten-Lyons, D., Woltjer, R.L., Dodge, H., Nixon, R., Vorobik, R., Calvert, J.F., Leahy, M., Montine, T., Kaye, J., 2009. Factors associated with resistance to dementia despite high Alzheimer disease pathology. Neurology 72, 354–360.

Greco, V., Naletova, I., Ahmed, I.M.M., Vaccaro, S., Messina, L., La Mendola, D., Bellia, F., Sciuto, S., Satriano, C., Rizzarelli, E., 2020. Hyaluronan-carnosine conjugates inhibit Aβ aggregation and toxicity. Sci. Rep. 10, 15998.

Honary, S., Zahir, F., 2013. Effect of zeta potential on the properties of nano-drug delivery systems - a review (Part 1). Trop. J. Pharm. Res. 12, 255–264.

Jiang, Z., Dong, X., Yan, X., Liu, Y., Zhang, L., Sun, Y., 2018. Nanogels of dual inhibitor-modified hyaluronic acid function as a potent inhibitor of amyloid β-protein aggregation and cytotoxicity. Sci. Rep. 8, 3505.

Khatun, Z., Nurunnabi, M., Nafiujjaman, M., Reeck, G.R., Khan, H. A., Cho, K.J., Lee, Y., 2015. A hyaluronic acid nanogel for photo–chemo theranostics of lung cancer with simultaneous light-responsive controlled release of doxorubicin. Nanoscale 7, 10680–10689.

Li, J., Mooney, D.J., 2016. Designing hydrogels for controlled drug delivery. Nat. Rev. Mater. 1, 16071.

Lin, C.-Y., Perche, F., Ikegami, M., Uchida, S., Kataoka, K., Itaka, K., 2016. Messenger RNA-based therapeutics for brain diseases: An animal study for augmenting clearance of beta-amyloid by intracerebral administration of neprilysin mRNA loaded in polyplex nanomicelles. J. Control. Release 235, 268–275.

Mahmoudi, M., 2018. Debugging Nano-Bio Interfaces: Systematic Strategies to Accelerate Clinical Translation of Nanotechnologies. Trends Biotechnol. 36, 755–769.

Mahmoudi, M., Quinlan-Pluck, F., Monopoli, M.P., Sheibani, S., Vali, H., Dawson, K.A., Lynch, I., 2013. Influence of the physiochemical properties of superparamagnetic iron oxide nanoparticles on amyloid β protein fibrillation in solution. ACS Chem. Neurosci. 4, 475–485.

Marschütz, M.K., Bernkop-Schnürch, A., 2002. Thiolated polymers: self-crosslinking properties of thiolated 450 kDa poly(acrylic acid) and their influence on mucoadhesion. Eur. J. Pharm. Sci. 15, 387–394.

Mucke, L., Selkoe, D.J., 2012. Neurotoxicity of amyloid β-protein: synaptic and network dysfunction, Cold Spring Harb. Perspect. Med. 2, a006338–a006338.

Murphy, M.P., LeVine 3rd, H., 2010. Alzheimer's disease and the amyloid-beta peptide. J. Alzheimers. Dis. 19, 311–323.

Oliveri, V., Bellia, F., Pietropaolo, A., Vecchio, G., 2015. Unusual Cyclodextrin Derivatives as a New Avenue to Modulate Self- and Metal-Induced Aβ Aggregation. Chem. – A Eur. J. 21, 14047–14059.

Online, V.A., Beuerman, R.W., Lakshminarayanan, R., Dwivedi, N., Ramakrishna, S., 2014. Role of size of drug delivery carriers in pulmonary and intravenous administration with emphasis on cancer therapeutics and lung-targeted drug delivery. RSC Adv. 4, 32673–32689.

Patrizia Cavazzoni, FDA's Decision to Approve New Treatment for Alzheimer's Disease, 2021. https://www.fda.gov/drugs/news-events-human-drugs/fdas-decision-approve-new-treatment-alzheimers-disease.

Rodell, C.B., MacArthur Jr., J.W., Dorsey, S.M., Wade, R.J., Wang, L.L., Woo, Y.J., Burdick, J.A., 2015. Shear-Thinning Supramolecular Hydrogels with Secondary Autonomous Covalent Crosslinking to Modulate Viscoelastic Properties In Vivo. Adv. Funct. Mater. 25, 636–644.

Sakulkhu, U., Mahmoudi, M., Maurizi, L., Salaklang, J., Hofmann, H., 2014. Protein corona composition of superparamagnetic iron oxide nanoparticles with various physico-chemical properties and coatings. Sci. Rep. 4, 5020.

Schweiger, C., Pietzonka, C., Heverhagen, J., Kissel, T., 2011. Novel magnetic iron oxide nanoparticles coated with poly(ethylene imine)-g-poly(ethylene glycol) for potential biomedical application: synthesis, stability, cytotoxicity and MR imaging. Int. J. Pharm. 408, 130–137.

Seliktar, D., 2012. Designing Cell-Compatible Hydrogels for Biomedical Applications, Science (80-.). 336, 1124 LP – 1128.

Sheervalilou, R., Shirvaliloo, M., Sargazi, S., Ghaznavi, H., 2021. Recent advances in iron oxide nanoparticles for brain cancer theranostics: from in vitro to clinical applications. Expert Opin. Drug Deliv. 1–29.

Shevtsov, M.A., Nikolaev, B.P., Yakovleva, L.Y., Marchenko, Y.Y., Dobrodumov, A.V., Mikhrina, A.L., Martynova, M.G., Bystrova, O.A., Yakovenko, I.V., Ischenko, A.M., 2014. Superparamagnetic iron oxide nanoparticles conjugated with epidermal growth factor (SPION-EGF) for targeting brain tumors. Int. J. Nanomed. 9, 273–287.

Simulescu, V., Mondek, J., Kalina, M., Pekař, M., 2015. Kinetics of long-term degradation of different molar mass hyaluronan solutions studied by SEC-MALLS. Polym. Degrad. Stab. 111, 257–262.

Snetkov, P., Zakharova, K., Morozkina, S., Olekhnovich, R., Uspenskaya, M., 2020. Hyaluronic Acid: The Influence of Molecular Weight on Structural, Physical, Physico-Chemical, and Degradable Properties of Biopolymer. Polymers (Basel) 12, 1800.

Stephen, Z.R., Kievit, F.M., Zhang, M., 2011. Magnetite nanoparticles for medical MR imaging. Mater. Today. 14, 330–338.

Su, H., Han, X., He, L., Deng, L., Yu, K., Jiang, H., Wu, C., Jia, Q., Shan, S., 2019. Synthesis and characterization of magnetic dextran nanogel doped with iron oxide nanoparticles as magnetic resonance imaging probe. Int. J. Biol. Macromol. 128, 768–774.

Sun, J., Xie, W., Zhu, X., Xu, M., Liu, J., 2018. Sulfur Nanoparticles with Novel Morphologies Coupled with Brain-Targeting Peptides RVG as a New Type of Inhibitor Against Metal-Induced Aβ Aggregation. ACS Chem. Neurosci. 9, 749–761.

Tian, H., He, Z., Sun, C., Yang, C., Zhao, P., Liu, L., Leong, K.W., Mao, H.-Q., Liu, Z., Chen, Y., 2018. Uniform Core-Shell Nanoparticles with Thiolated Hyaluronic Acid Coating to Enhance Oral Delivery of Insulin. Adv. Healthc. Mater. 7, e1800285.

Tosi, G., Pederzoli, F., Belletti, D., Vandelli, M.A., Forni, F., Duskey, J.T., Ruozi, B., 2019. Chapter 2 - Nanomedicine in Alzheimer's disease: Amyloid beta targeting strategy. In: Sharma, A., H.S.B.T.-P. in B.R. Sharma (Eds.) Nanoneuroprotection and Nanoneurotoxicology, Elsevier, pp. 57–88.

Trombino, S., Servidio, C., Curcio, F., Cassano, R., 2019. Strategies for Hyaluronic Acid-Based Hydrogel Design in Drug Delivery. Pharmaceutics 11, 407.

Valle-Delgado, J.J., Alfonso-Prieto, M., de Groot, N.S., Ventura, S., Samitier, J., Rovira, C., Fernàndez-Busquets, X., 2010. Modulation of Abeta42 fibrillogenesis by glycosaminoglycan structure. FASEB J. 24, 4250–4261.

Vilella, A., Belletti, D., Sauer, A.K., Hagmeyer, S., Sarowar, T., Masoni, M., Stasiak, N., Mulvihill, J.J.E., Ruozi, B., Forni, F., Vandelli, M.A., Tosi, G., Zoli, M., Grabrucker, A.M., 2018. Reduced plaque size and inflammation in the APP23 mouse model for Alzheimer's disease after chronic application of polymeric nanoparticles for CNS targeted zinc delivery. J. Trace Elem. Med. Biol. 49, 210–221.

Wang, Y.-X.-J., 2011. Superparamagnetic iron oxide based MRI contrast agents: Current status of clinical application. Quant Imaging Med. Surg. 1, 35–44.

Zagorski, M.G., Yang, J., Shao, H., Ma, K., Zeng, H., A.B.T.-M. in E. Hong, 1999. Methodological and chemical factors affecting amyloid β peptide amyloidogenicity, in: Amyloid, Prions, and Other Protein Aggregates, Academic Press, pp. 189–204.

Zhang, P., Hu, L., Yin, Q., Zhang, Z., Feng, L., Li, Y., 2012. Transferrin-conjugated polyphosphoester hybrid micelle loading paclitaxel for brain-targeting delivery: Synthesis, preparation and in vivo evaluation. J. Control. Release. 159, 429–434.

Zhu, H., Tao, J., Wang, W., Zhou, Y., Li, P., Li, Z., Yan, K., Wu, S., Yeung, K.W.K., Xu, Z., Xu, H., Chu, P.K., 2013. Magnetic, fluorescent, and thermo-responsive Fe3O4/rare earth incorporated poly(St-NIPAM) core-shell colloidal nanoparticles in multimodal optical/magnetic resonance imaging probes. Biomaterials 34, 2296–2306.